

# Multiband Adaptive Impedance Compensation Methods for Spatially Robust Capacitive Power Transfer Systems

Masoud Ahmadi<sup>1</sup>, Hoda Dadashzadeh<sup>2</sup>, Loïc Markley<sup>3</sup>, *Senior Member, IEEE*,  
and Thomas Johnson<sup>4</sup>, *Member, IEEE*

**Abstract**—This study aims to compare the merits of using both adaptive load resistance and adaptive frequency for impedance compensation in capacitive power transfer (CPT) systems. An adaptive load and frequency-band-switching compensation method is presented that achieves spatial robustness in a CPT system. The method complies with spectrum constraints that limit wireless power transfer to the discrete industrial, scientific, and medical (ISM) frequency bands. Coarse impedance control is obtained by switching frequencies, and fine impedance control is obtained by changing load resistance. The method is verified experimentally in a dual-band CPT system operating at two octave-spaced ISM bands: 13.56 and 27.12 MHz. The system is comprised of a six-plate CPT link, class-E inverters, and class-E self-synchronous rectifiers. Adaptive load compensation is implemented at the output of the rectifier. Experimental results show that, with frequency and load compensation, load power can be held constant over a spatial gap that ranges from 4.0 to 16.0 cm. Results show that the dual-band operation extends the spatial bandwidth of the system by 50% compared with a single frequency system operating at 13.56 MHz.

**Index Terms**—Adaptive frequency, adaptive load, capacitive power transfer (CPT), impedance compensation, multiband wireless power transfer.

## I. INTRODUCTION

CAPACITIVE power transfer (CPT) systems use resonant coupling to transfer power between a transmitter and a receiver. The resonant coupling network is typically designed to operate with a particular set of source and load impedances and at a particular transmission distance. To maximize the operating distance, the coupled resonators are matched when the critical coupling condition is met. If the spatial alignment of the transmitter and receiver is changed from the critically coupled configuration, then the coupling coefficient and impedances at the port terminals change. These spatial

impedance changes from critical coupling degrade the overall power efficiency of the system and change load power. Methods to compensate for spatial impedance changes are, therefore, very important to maintain high efficiency and regulated (constant) load power.

Frequency tracking has been proposed as a method to compensate for reactive changes due to spatial variation. This technique varies the operating frequency to maintain high system efficiency and regulate load power over variable distances [1], [2], [3], [4], [5], [6]. However, the frequency range required for compensation can often exceed the available bandwidth of the operating frequency band. For example, the ISM frequency bands centered at 6.78, 13.56, 27.12, and 40.68 MHz all have the fractional bandwidths of less than 1.2% (30, 14, 326, and 40 kHz, respectively). As a result, methods that vary frequency to compensate for spatial changes are unlikely to be compliant with the limited bandwidth of an ISM band. Frequency compensation is also limited to the overcoupled regime (i.e., at separation distances below the critically coupling distance) where efficient power transfer can be obtained by tracking a bifurcated frequency response.

Another impedance compensation method is to use an adjustable matching network. Examples include a switched bank of capacitors and inductors [7], [8], [9], [10] or an active circuit to vary reactance [11], [12], [13]. In these systems, a controller iteratively adjusts the matching network to find the best power transfer conditions. The primary challenge with adjustable matching networks is designing circuits that maintain high-quality factor and high-power capability, such that power efficiency is not significantly impacted.

The method of adaptive load resistance can also be used to compensate for spatial changes [14], [15], [16], [17]. This method is typically implemented by changing the load resistance at the output of the rectifier [18], [19], [20]. A change in load resistance also changes the input reactance of the rectifier, and the reactance change should be constrained to maintain high efficiency in the CPT link.

In this article, a method of combining adaptive load compensation with frequency band switching is investigated to enhance the spatial robustness of a CPT system (see Fig. 1). The operating frequencies are constrained to ISM frequency bands that are compatible with regulatory limitations that restrict operation to narrow channels. In other words, frequency compensation is restricted to discrete frequencies, rather than varying frequency continuously. In this way,

Manuscript received 8 September 2023; revised 16 January 2024; accepted 27 February 2024. Date of publication 7 March 2024; date of current version 4 June 2024. This work was supported in part by the Natural Sciences and Engineering Research Council of Canada (NSERC), in part by the Canada Foundation for Innovation (CFI), in part by the British Columbia Knowledge Development Fund (BCKDF), and in part by the National Research Council (NRC). Recommended for publication by Associate Editor Dylan Dah Chuan Lu. (Corresponding author: Masoud Ahmadi.)

Masoud Ahmadi, Loïc Markley, and Thomas Johnson are with the School of Engineering, The University of British Columbia, Kelowna, BC V1V 1V7, Canada (e-mail: mdsai@student.ubc.ca; loic.markley@ubc.ca; thomas.johnson@ubc.ca).

Hoda Dadashzadeh is with Fortinet, Burnaby, BC V5C 6C6, Canada (e-mail: dadashzadehhoda@gmail.com).

Color versions of one or more figures in this article are available at <https://doi.org/10.1109/JESTPE.2024.3374330>.

Digital Object Identifier 10.1109/JESTPE.2024.3374330

2168-6777 © 2024 IEEE. Personal use is permitted, but republication/redistribution requires IEEE permission.

See <https://www.ieee.org/publications/rights/index.html> for more information.

TABLE I  
[=SUMMARY OF SPATIAL IMPEDANCE COMPENSATION METHODS REPORTED IN THE LITERATURE

Ref.	Compensation Method	Frequency (MHz)	Critical Coupling Distance (cm)	Constant Power Range (cm)	Constant Efficiency Range (cm)	Configuration
[1]	Continuous Frequency Tracking	6.10 – 6.80	50.0	10.0 – 50.0	10.0 – 50.0	IPT resonators - full system <sup>1</sup>
[2]	Continuous Frequency Tracking	6.50 – 9.50	80.0	10.0 – 80.0	10.0 – 80.0	IPT resonators
[7]	Adaptive Matching Network	13.56	20.0	N.A.	6.0 – 29.0	IPT Resonators
[12]	Adaptive Matching Network	13.56	12.0	12.0 – 18.0	12.0 – 13.0	CPT resonators - full system
[16]	Adaptive Load	6.78	0.20*	N.A.	0.15* – 0.30*	IPT resonators - full system
[17]	Adaptive Load	13.56	0.12*	N.A.	0.05* – 0.17*	IPT resonators - full system
This Work	Adaptive Load and Frequency Switching	13.56 / 27.12	13.6 / 9.6	6.0 – 16.0	6.0 – 16.0	CPT resonators - full system

\* Denotes coupling coefficient instead of distance.

<sup>1</sup> The term "full system" refers to a combination of an inverter, WPT resonators, and rectifier working together as a complete unit.

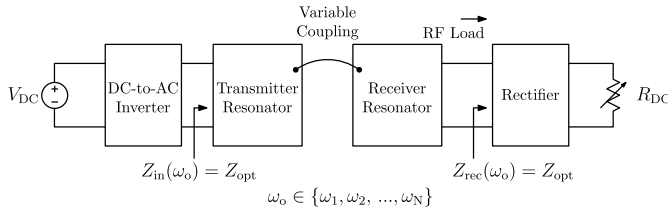


Fig. 1. Proposed compensation method: spatial changes modify resonator coupling, which is compensated by adjusting a variable load  $R_{dc}$  for fine spatial compensation and by frequency band switching for coarse spatial compensation. The operating frequency  $\omega_o$  is selected from a set of industrial, scientific, and medical (ISM) bands  $\omega_1, \omega_2, \dots, \omega_N$ . The objective of compensation is to maintain a constant impedance at the inverter and rectifier RF ports.

frequency compensation implements coarse impedance control by switching ISM bands, and an adaptive load resistance implements fine impedance control within each frequency band. This enables the multiband adaptive load compensation method to maintain critical coupling over a large spatial range compared with uncompensated systems that would have critically coupled, overcoupled, and undercoupled regions of operation over the same spatial range. Although multiband WPT systems have been proposed before that work within the regulated frequency bandwidths [21], [22], [23], [24], [25], [26], these systems use the additional frequency band for supporting data communication and control rather than using alternate frequencies for impedance compensation. Therefore, the method of using both frequency and load impedance to compensate for spatial changes is new and motivates the work described in this article.

A comparison of the proposed compensation method compared with other published work in the literature is shown in Table I. Frequency tracking-based methods are effective

within a specific range, particularly when the resonators are overcoupled under a fixed load, where frequency bifurcation occurs. On the other hand, approaches involving an adaptive matching network and an adaptive load primarily emphasize maximizing system efficiency but may compromise delivering constant load power. The method presented in this article addresses these challenges by enabling the maintenance of a critically coupled response. This, in turn, ensures a constant input impedance, resulting in sustained high system efficiency and constant load power.

A theoretical analysis of the adaptive load and frequency-band-switching method is presented. The analysis is based on modeling the CPT as a bandpass filter network that consists of resonators coupled by impedance inverters [27]. The filter theory approach is used to show how changing the load resistance can maintain a constant input impedance at the transmit port over a limited spatial range where changes in the resonant frequency of the coupling resonators are small. The impedance inverter model also shows how the spatial range can be extended by switching frequency bands. Since practical wireless power systems use an adaptive load at the dc output port of the rectifier, an analysis is shown to study the relationship between load resistance and input impedance in a class-E rectifier. The analysis shows that the range of load resistance change is limited by reactive changes at the input of rectifier. In Section VII of this article, the concepts are applied to the design of a six-plate CPT system that uses two octave-spaced ISM frequency bands at 13.56 and 27.12 MHz.

## II. SIX-PLATE STRUCTURE

The structure of a six-plate CPT link is shown in Fig. 2 and is comprised of four concentric circular electrodes enclosed

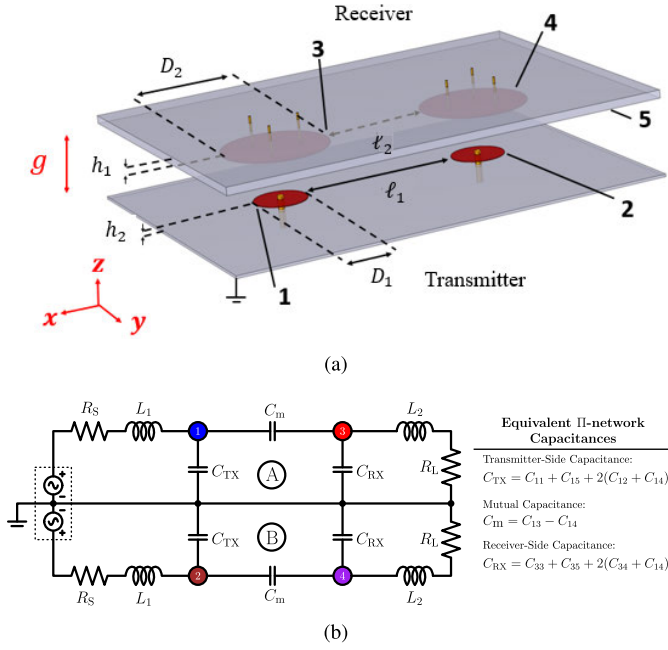


Fig. 2. Six-plate CPT coupling link. (a) Geometry of the electrodes. (b) Equivalent circuit composed of two identical half-circuits connected to differential source and load.

between two large shielding plates. The electrodes in the transmitter are labeled as 1 and 2, while the receive electrodes are labeled 3 and 4. The two transmitter electrodes are aligned with the two receiver electrodes and separated by an air gap of  $g$ . The transmit electrodes and the receive electrodes are also separated from the shielding plates by distances of  $h_1$  and  $h_2$ , respectively.

When the transmitter electrodes are identical and the receiver electrodes are identical, the network can be reduced to an equivalent half-circuit comprised of two  $\Pi$  networks of capacitances, as shown in Fig. 2(b). Clements et al. [28] established a relationship between the equivalent capacitances in the half-circuits  $C_{TX}$ ,  $C_m$ , and  $C_{RX}$ , and the interelectrode capacitances, which are included in Fig. 2(b) for reference. Note that the capacitance between a pair of conductors  $i$  and  $j$  is identified as  $C_{ij}$ , and the capacitance between a conductor  $i$  and the grounded transmitter shielding plate is identified as  $C_{ii}$ . Half-circuit A shown in Fig. 2(b) is used for the remainder of this article.

### III. LOAD AND FREQUENCY COMPENSATION

In this section, a filter synthesis methodology [27] is used to derive expressions for the required load resistance to compensate for changes in the gap distance  $g$  of a CPT link. A discussion of how frequency switching can extend the range of load compensation is also presented.

The analysis begins with the equivalent  $\Pi$  network of capacitances, as shown in Fig. 3(a). Note that all capacitances in the  $\Pi$  network ( $C_{TX}$ ,  $C_m$ , and  $C_{RX}$ ) depend on the separation gap distance  $g$  between the transmitter and the receiver. Furthermore,  $C_{TX}$  and  $C_{RX}$  are, in general, different, and an asymmetry factor is defined as  $m = (C_{RX} + C_m)/(C_{TX} + C_m)$ . In the next step, two series inductors,  $L_1$  and  $L_2$ , are added to the half-circuit in Fig. 3(a). The CPT link with matching inductors can be modeled as a filter. An equivalent circuit

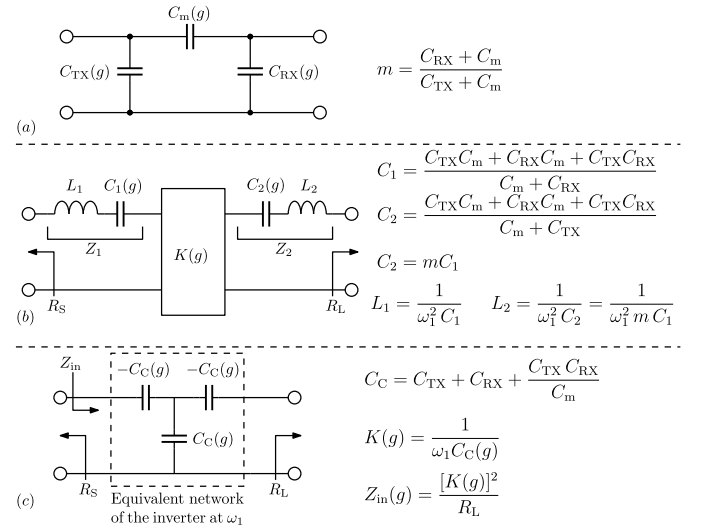


Fig. 3. Steps to transform an equivalent half-circuit model into an impedance inverter. (a) Equivalent half-circuit model of a CPT link. Matching inductors,  $L_1$  and  $L_2$ , are added to the circuit. (b) Half-circuit with matching inductors can be modeled as an equivalent filter network consisting of two series resonators and an impedance inverter  $K(g)$ . Expressions are given to relate the physical capacitances in (a) to the equivalent circuit in (b). The matched CPT filter circuit has a center frequency of  $\omega_1$ . At the center frequency, the series resonators have zero impedance, and the circuit in (b) simplifies to an impedance inverter  $K(g)$  whose impedance is a function of gap distance. (c) Impedance inverter can be replaced by its lumped element equivalent network at  $\omega_1$ .

model of the filter network is shown in Fig. 3(b), where two series resonators are coupled by an impedance inverter  $K(g)$ . Equations for the circuit elements are given in Fig. 3(b) and show how the physical capacitances in Fig. 3(a) relate to the equivalent circuit model. The inverter impedance  $K(g)$  is equal to  $1/(\omega_1 C_C)^2$ , where  $C_C$  is given by  $C_{TX} + C_{RX} + (C_{TX} C_{RX}/C_m)$  [27].

The filter network has a bandpass frequency response with a center frequency  $\omega_1$ . At  $\omega_1$ , the series resonators have zero impedance, and the filter network simplifies to an impedance inverter whose impedance changes as a function of the gap distance. The circuit model at  $\omega_1$  is shown in Fig. 3(c). Using this model, the input impedance to the CPT link terminated in a load resistance  $R_L$  is

$$Z_{in}(g) = \frac{K(g)^2}{R_L} = \frac{1}{[\omega_1 C_C(g)]^2 R_L}. \quad (1)$$

Equation (1) provides an analytical framework to explain how load impedance and frequency can be used to compensate for changes in gap distance. With reference to Fig. 4, consider a CPT system that has both an adjustable load resistance as well as frequency band switching to compensate for spatial capacitance changes. At a frequency  $\omega_1$ , suppose the system is matched for critical coupling at a specific gap distance  $g_{opt,1}$ . The values of the series matching inductors,  $L_1$  and  $L_2$ , are selected to resonate at  $\omega_1$  for a critical coupling separation distance of  $g_{opt,1}$ . Under this condition, the optimum load resistance required to obtain an input impedance  $Z_{opt}$  is

$$R_{L,opt} = \frac{1}{[\omega_1 C_C(g_{opt,1})]^2 Z_{opt}}. \quad (2)$$

Next, consider a change in gap distance in the neighborhood of  $g_{\text{opt},1}$ . As gap distance changes, the value of  $C_C(g)$  changes, and the load resistance  $R_L(g)$  can be adjusted to maintain a constant  $\omega_1^2 C_C(g)^2 R_L(g)$  product, such that the input impedance at the source side is constant. Note that although (1) appears to be satisfied by the adjustment in load resistance, it is important to recall that this equation assumes that the series resonators  $L_1 C_1$  and  $L_2 C_2$  are resonant at  $\omega_1$ . When  $g = g_{\text{opt},1}$ , the resonance condition is satisfied; however, as the gap distance deviates from  $g_{\text{opt},1}$ , the resonators start to become mistuned, because  $C_1$  and  $C_2$  also change, as the gap distance changes. Consequently, a small residual reactance is introduced at the input port, as the gap distance moves away from  $g_{\text{opt},1}$ . As a result, changes in the separation gap cannot be fully compensated by adjusting the load resistance. There is, however, a distance range, referred to as the compensation range, where the residual reactances are small, and where resonators can still be approximated as short circuits at the operating frequency  $\omega_1$ . Over the compensated range, (1) can be used to find the corresponding load resistance that maintains a constant input impedance of  $Z_{\text{opt}}$ . The compensated load resistance  $R_{L,\text{opt}}(g)$  is approximated by

$$R_{L,\text{opt}}(g) \approx \frac{1}{[\omega_1 C_C(g)]^2 Z_{\text{opt}}}. \quad (3)$$

Note that, due to the dependence of  $C_C$  on the link capacitances [see Fig. 3(b)], the optimal resistances required for compensation depend on the CPT link capacitances. As transmission distance varies, the transmitter- and receiver-side capacitances  $C_{\text{TX}}$  and  $C_{\text{RX}}$  remain relatively constant, while the mutual capacitance  $C_m$  varies significantly, as shown in a later example in Section V. Consequently, the value of the optimal resistances becomes primarily dependent on the mutual capacitance. In addition, the extent of the compensated distance range depends on the spatial sensitivity of the capacitances associated with the CPT plate geometry.

For distances outside the compensated distance range, the variation in the resonant frequencies of the resonators is too large, and the adaptive load technique can no longer maintain a constant input impedance. As a way to extend the compensation range, the operating frequency of the CPT link can be changed. Consider operation at a second frequency  $\omega_2$ . In order to restore the network to an equivalent state, then it is also necessary to adjust the values of the matching inductors to maintain the reactance of all elements in the network. Adjustment to the matching inductors can be made using two switches, as shown in Fig. 4. The required inductances to establish resonance at  $\omega_2$  are  $L'_1$  and  $L'_2$ . The system shown in Fig. 4 assumes that  $\omega_1 > \omega_2$ ; therefore,  $L'_1 > L_1$  and  $L'_2 > L_2$ .

The operating frequencies  $\omega_1$  and  $\omega_2$  must lie within the regulatory frequency bands allocated for WPT systems. In addition, a constant input impedance of  $Z_{\text{opt}}$  must be maintained for both frequency bands. Once the two frequency bands are selected, a second critically coupled gap distance  $g_{\text{opt},2}$  can be defined, such that the input impedance at  $\omega_2$  is  $Z_{\text{opt}}$ . Similar to operation at  $\omega_1$ , load compensation can be applied at  $\omega_2$  to form a second compensated spatial range that overlaps with the first compensation range. In this

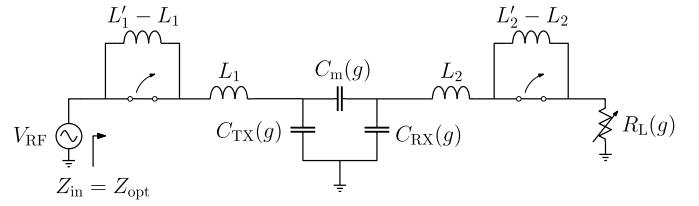


Fig. 4. Basic configuration of the proposed adaptive load and frequency-band-switching compensation technique applied to a CPT system. The link at each operating frequency has fixed matching inductors and a variable load resistance that is used to maintain a constant link input impedance. In general, this method can be extended to a system that has more than two frequencies of operation.

way, band switching is used to implement coarse impedance compensation, while load compensation is used to implement fine impedance compensation. When the compensated ranges of both frequency bands are combined, a large range of impedance compensation can be obtained. Note that a practical frequency-band-switching system would include power control to ramp the power down before switching frequencies to avoid generating unstable load conditions that could occur during the frequency switching intervals. In this way, the system is assumed to be quasi-static, such that potential unstable load conditions are avoided.

#### IV. RESONATOR QUALITY FACTOR

The analysis in Section III assumed that all network components are ideal. However, in practice, resonators exhibit losses, and their inherent parasitic resistances can impact load compensation. The synthesis of canonical filter structures, including losses from finite quality factor ( $Q$ ), is well studied in the literature [29], [30], [31]. Using the same synthesis method in Section III, expressions are derived for the optimal load compensation resistance for CPT systems with finite- $Q$  resonators.

The model of the CPT system with nonideal resonators is illustrated in Fig. 5(a), where  $R_1$  and  $R_2$  represent the parasitic resistances of the resonators. At resonance and at the critically coupled transmission distance  $g_{\text{opt}}$ , the series resonators become short circuits, simplifying the equivalent circuit of the CPT link to the configuration shown in Fig. 5(b). The network is comprised of series resistances separated by an impedance inverter. The input impedance of the link in (1) can be modified to account for the parasitic load resistances of the resonators

$$Z_{\text{in}} = R_1 + \frac{[K(g)]^2}{R_2 + R_L}. \quad (4)$$

An interesting observation is that (4) shows how the impedance inverter  $K(g)$  desensitizes changes in input impedance for resonators with finite  $Q$ . The first term increases, while the second term decreases because of the impedance inversion through the inverter. Furthermore, since power efficiency is important, high- $Q$  resonators are preferred, and the values of  $R_1$  and  $R_2$  are expected to be small. Consequently, the optimum load resistance for finite  $Q$  resonators is not expected to deviate significantly from the ideal value given in (3).



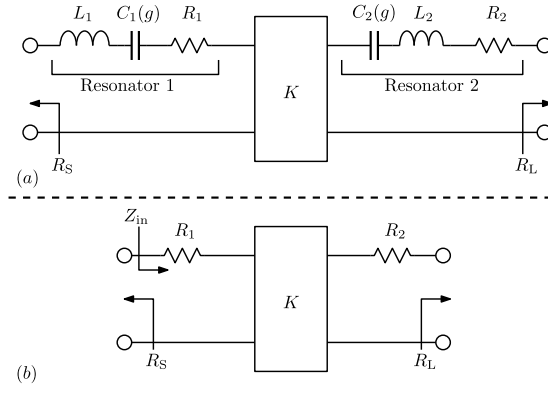


Fig. 5. (a) Loss due to the finite quality factor of the resonators is modeled by series resistances  $R_1$  and  $R_2$ . (b) Impact of parasitics on the input impedance of the link is demonstrated.

TABLE II

SINGLY TERMINATED SECOND-ORDER FILTER COEFFICIENTS FOR A BUTTERWORTH FILTER RESPONSE

$g_0$	$g_1$	$g_2$	$g_3$	$m$
0	1.4142	0.7071	1.0000	2.0000

## V. DESIGN EXAMPLE

In this section, an example of a six-plate CPT system is shown to verify the compensation method. A filter-based design methodology is used to determine the values of the resonator components based on the operating frequency and the required port resistances [27], [29], [32].

The first step is to select a network topology that is appropriate for the design. The singly terminated network topology is useful for systems that are driven by high-efficiency power sources [29], [33], [34]. High-efficiency sources are often modeled as ideal current or voltage sources and assume that the amplifier is 100% efficient with no significant dissipation. In this work, high-efficiency class-E amplifiers are used along with singly terminated filter prototypes.

For a critically coupled (maximally flat) frequency response at the center frequency  $\omega_1$ , Butterworth filter coefficients are used [27]. The normalized filter coefficients for a second-order singly terminated Butterworth filter are given in Table II. The coefficients are  $g_0$ ; the source resistances, which is zero for a singly terminated network,  $g_1$  and  $g_2$  are filter reactances, and  $g_3$  is the normalized load resistance and equal to 1  $\Omega$ . Using the filter theory approach, the coefficients are impedance scaled by  $k_z$  and transformed into a bandpass filter with a center frequency of  $\omega_1$ .

An impedance scaling factor of  $k_z = R_L$  is used for the filter synthesis, where  $R_L$  is the load resistance (or equivalently,  $R_L$  is the rectifier input impedance when the load is a rectifier). Note that the scaling factor is also equal to the input impedance of the filter network at the center frequency  $\omega_1$ . Under this impedance scaling, the singly terminated network presents a resistance ( $Z_{in}$ ) of  $R_L$  to the source for the critical coupling gap condition in the CPT link. Using the expressions in Fig. 3(c) and solving for the condition  $Z_{in} = R_L$ , the impedance inverter is

$$K(g_{opt}) = R_L = k_z = \frac{1}{\omega_1 C_C(g_{opt})}. \quad (5)$$

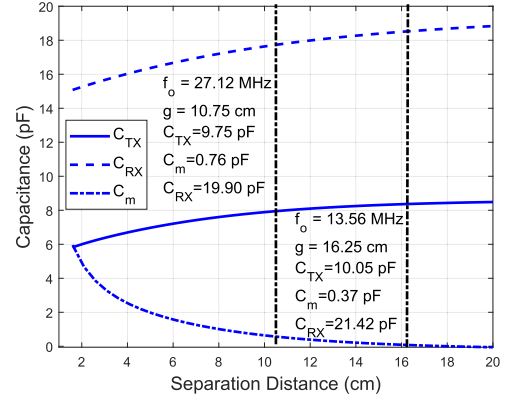


Fig. 6. Equivalent half-circuit capacitances as a function of gap distance for the six-plate structure. Capacitances are derived from a 3-D electrostatic simulation with  $h_1 = 1.2$  cm and  $h_2 = 2.4$  cm.

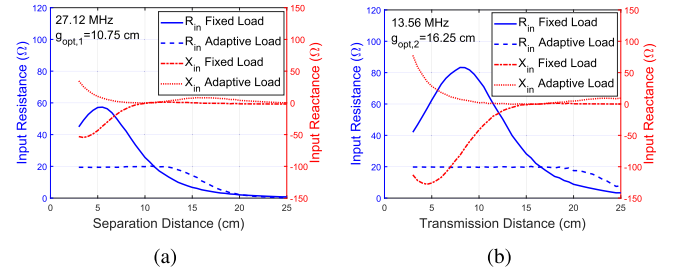


Fig. 7. Input resistance and reactance of the CPT links under fixed-load and adaptive load conditions are plotted versus the separation distance  $g$ . The response shown in (a) is for the link operating at 27.12 MHz and (b) is for the link at 13.56 MHz.

Another equivalent expression for the inverter impedance can be derived from the scaled canonical filter prototype, where

$$K(g_{opt}) = k_z \sqrt{\frac{g_1}{mg_2}} \quad (6)$$

and the asymmetry factor is given by

$$m = \frac{g_1}{g_2}. \quad (7)$$

For the values given in Table II,  $m = 2.0$ .

The six-plate geometry used in this example has the following physical parameters. With reference to Fig. 2(a), the diameters of the transmitter disks ( $D_1$  and  $D_2$ ) are 10 cm, and the diameters of the receiver disks ( $D_3$  and  $D_4$ ) are 20 cm. The shielding back plates (electrodes 5 and 6) are rectangular and  $84 \times 61$  cm<sup>2</sup> in size. Each pair of disks, (1, 2) and (3, 4), are spaced 40 cm apart center to center; therefore,  $\ell_1 = 20$  cm and  $\ell_2 = 10$  cm.

The ISM bands chosen for the design are centered at 13.56 and 27.12 MHz, and the load resistance  $R_L$  is 20  $\Omega$ . The mutual capacitances in the six-plate system were found through a 3-D electrostatic simulation using COMSOL. The distance to the shield plates are  $h_1 = 1.2$  cm and  $h_2 = 2.4$  cm to obtain an asymmetry factor as close to  $m = 2$  as possible.

The half-circuit capacitances as a function of gap distance  $g$  are shown in Fig. 6. For 27.12 MHz, the fixed-load critical coupling distance is 10.75 cm, and for 13.56 MHz, this distance is 16.25 cm. From 10.75 to 16.25 cm,  $C_{TX}$ ,  $C_m$ , and  $C_{RX}$  vary by 3.1%, 51.3%, and 7.6%. It is clear that the mutual

TABLE III  
DESIGN PARAMETERS FOR THE 27.12-MHz CPT SYSTEM

Unit	Parameter	Value	Parameter	Value
PA	$L_{CH}$	1.50 $\mu\text{H}$	$R$	47 $\Omega$
	$C_P$	55.0 pF	$C$	35.0 pF
	$L_T$	0.58 $\mu\text{H}$	$C_j$	100.0 nF
	$C_T$	58.7 pF	$R_1$	25 $\Omega$
	$L_{SW}$	0.13 $\mu\text{H}$	$R_2$	15 $\Omega$
	$R_L$	20 $\Omega$	$V_{DD2}$	4.8 V
	$Q_{PA}$	5	$v_P$	4.0 V
	$V_{DD1}$	10	$D$	50%
	$C_{TX}$	9.75 pF	$h_1$	1.2 cm
	$C_m$	0.76 pF	$h_2$	2.4 cm
CPT Link	$C_{RX}$	19.90 pF	$\ell_1$	20.0 cm
	$L_1$	2.93 $\mu\text{H}$	$\ell_2$	10.0 cm
	$L_2$	1.60 $\mu\text{H}$	$D_1$	10.0 cm
	$Q_1 (Q_2)$	123.4 (147.7)	$D_2$	20.0 cm
	$C_b$	2.5 pF	$g_{opt,2}$	9.6 cm
	$m$	2.1		
	$K_C$	5.48%		
	$k_z$	21.75 $\Omega$		
	$K$	20.98 $\Omega$		
	$L_g$	455 nH		
Rectifier	$C_{56}$	33.0 pF		
	$L_f$	3.0 $\mu\text{H}$	$R_a$	500 $\Omega$
	$C_f$	24.0 pF	$R_{dc}$	35 $\Omega$
	$V_{DD3}$	4.8 V	$V_{DD4}$	1.5 V
	$C_{dc}$	10.0 nF		

TABLE IV  
DESIGN PARAMETERS FOR THE 13.56-MHz CPT SYSTEM

Unit	Parameter	Value	Parameter	Value
PA	$L_{CH}$	2.3 $\mu\text{H}$	$R$	47 $\Omega$
	$C_P$	120.0 pF	$C$	60.0 pF
	$L_T$	1.17 $\mu\text{H}$	$C_j$	100 nF
	$C_T$	117.4 pF	$R_1$	25 $\Omega$
	$L_{SW}$	0.24 $\mu\text{H}$	$R_2$	15 $\Omega$
	$R_L$	20 $\Omega$	$V_{DD1}$	4.8 V
	$Q_{PA}$	5	$v_P$	4.0 V
	$V_{DD1}$	10	$D$	50%
	$C_{TX}$	10.05 pF	$h_1$	1.2 cm
	$C_m$	0.37 pF	$h_2$	2.4 cm
CPT Link	$C_{RX}$	21.42 pF	$\ell_1$	20.0 cm
	$L'_1$	9.13 $\mu\text{H}$	$\ell_2$	10.0 cm
	$L'_2$	5.37 $\mu\text{H}$	$D_1$	10.0 cm
	$Q_1 (Q_2)$	125.0 (333.5)	$D_2$	20.0 cm
	$C_b$	2.5 pF	$g_{opt,2}$	13.6 cm
	$m$	2.1		
	$k_C$	2.40%		
	$k_z$	22.34 $\Omega$		
	$K$	21.42 $\Omega$		
	$L_g$	455 nH		
Rectifier	$C_{56}$	29.6 pF		
	$L_f$	6.3 $\mu\text{H}$	$R_a$	500 $\Omega$
	$C_f$	51.0 pF	$R_{dc}$	35 $\Omega$
	$V_{DD3}$	4.8 V	$V_{DD4}$	1.5 V
	$C_{dc}$	10.0 nF		

capacitance is the dominating factor in finding the value of optimal resistance. The design parameters for both frequency bands are summarized in Tables III and IV.

After completing the design for the condition of critical coupling, the impedance characteristics of the six-plate CPT link are evaluated under variable gap conditions. The impedance characteristics were compared between a system with a fixed-load resistance of 20  $\Omega$  and a system with a variable load providing adaptive load compensation. Circuit simulations in LTspice were used to evaluate load compensation, where the value of the load resistance was modified according to (3). The results are shown in Fig. 7, where the input resistance and reactance of the adaptive load links are plotted versus separation gap  $g$ . The input impedance of the fixed-load links is added for comparison. The input impedance is within 15% of 20  $\Omega$  for separation distances ranging from 4.5 to 14.0 cm at 27.12 MHz and from 7.0 to 20.0 cm at 13.56 MHz.

In Section VI, the analysis of the compensation methods is extended to include the implementation of the source and load using high-efficiency class-E circuits.

## VI. CLASS-E AMPLIFIER AND RECTIFIER

In this work, class-E circuits are used to implement high-efficiency amplifier and rectifier circuits. A class-E power amplifier will be introduced, and then, the principal of time-reversal duality will be used to reverse power flow and transform the amplifier into a class-E rectifier [35]. The RF input impedance of the rectifier is the load impedance that is presented to the CPT link. An analysis of the RF input

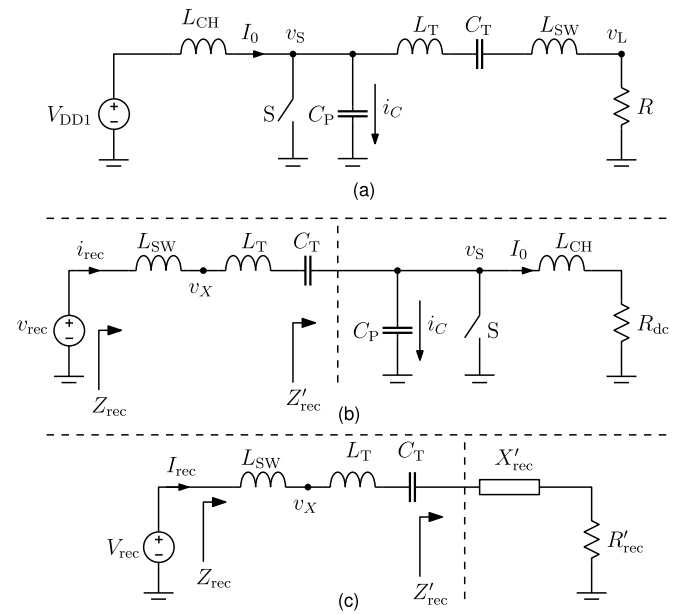


Fig. 8. Class-E amplifier and rectifier circuits. (a) Class-E amplifier. (b) Class-E rectifier obtained using time-reversal duality. (c) Equivalent circuit for the input impedance of the rectifier at the switching frequency  $\omega_1$ .

impedance for the adaptive load compensation method will then be presented.

The tuned single-ended class-E power amplifier is shown in Fig. 8(a). Two class-E PAs, one for each frequency band, were designed for an optimum load resistance of 20  $\Omega$ . The switch is an EPC2037 eGaN FET from Efficient Power Conversion (EPC) Technologies. The circuit diagram of the

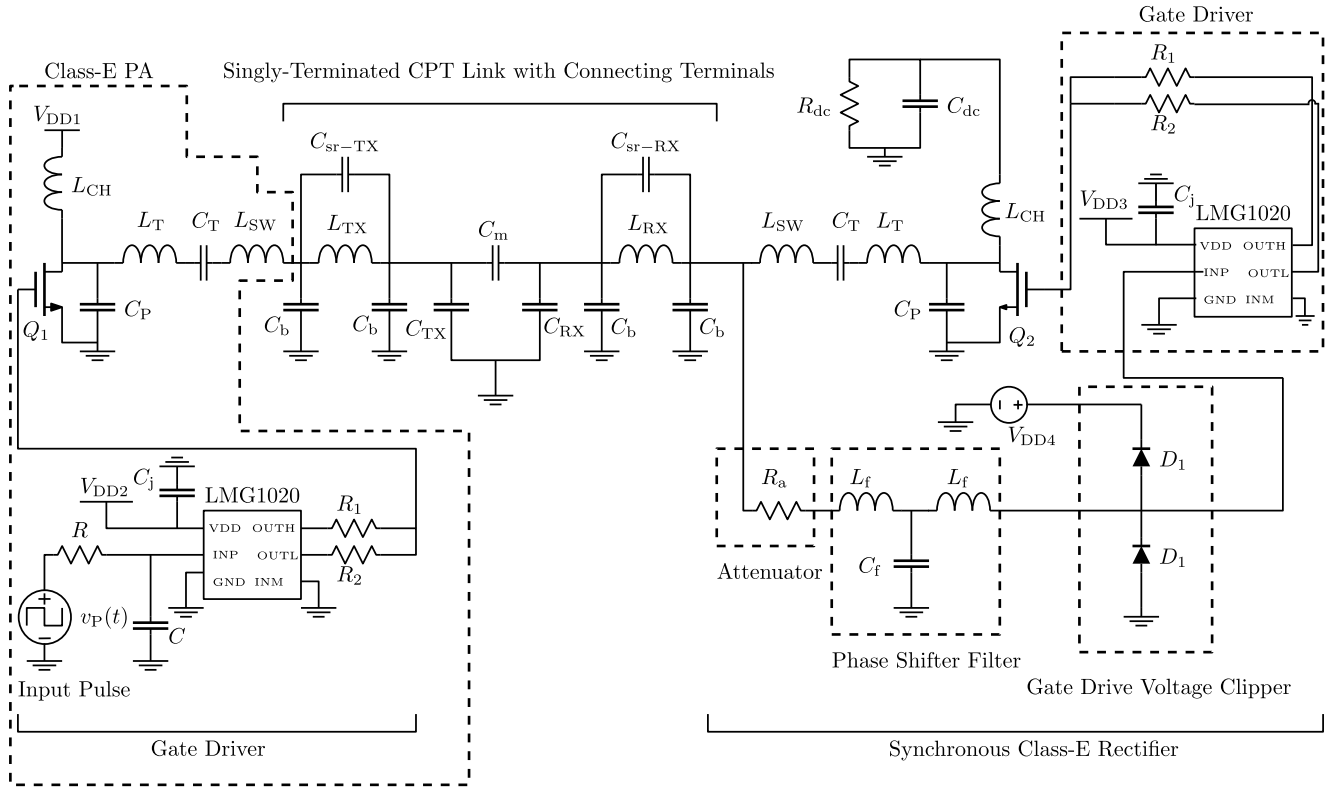


Fig. 9. Schematic of the overall CPT system, including the class-E amplifier, equivalent half-circuit for the six-plate CPT link, and the class-E rectifier. The CPT link includes matching inductors  $L_{TX,1}$  and  $L_{RX,1}$  and the parasitic capacitance in the inductors  $C_{sr-TX}$  and  $C_{sr-RX}$ . The inductors also include stray capacitance  $C_b$ , which models capacitance from terminals used to mount the inductors.

class-E amplifier is shown on the left-hand side of Fig. 9. Specifications for the EPC2037 include a maximum drain-source voltage of 100 V, a maximum continuous drain current of 1.7 A, and a gate-source threshold voltage of approximately 2.2 V [36]. The gate of the switch is driven by an LMG1020 gate driver from Texas Instruments. The input to the gate driver is a pulse generator ( $v_P$ ), and the signal is filtered by an RC low-pass filter that can be tuned to set the duty cycle of gate signal. There are two damping resistors,  $R_1$  and  $R_2$ , placed between the driver output terminals and the gate of the device. The damping resistors connect to the high and low drive transistors (FETs) in the LMG1020 driver. With a duty cycle ( $D$ ) of 50%, a 10% safety factor for peak drain-source voltage, and a series resonator quality factor ( $Q_{PA}$ ) of 5, the class-E power amplifiers can deliver an output power of up to 10 W for both frequency bands. The amplifier designs are summarized in Tables III and IV.

Using the principle of time-reversal duality, high-efficiency amplifiers can be transformed into equivalent high-efficiency rectifiers. The primary concept of time-reversal duality is to reverse the power flow through the circuit [35]. In the amplifier, dc input power is converted to RF output power, and the amplifier functions as an inverter. In the rectifier, RF power coupled through the CPT link is converted to a dc output that powers a load. The rectifier circuit dual obtained from the class-E amplifier is shown in Fig. 8(b). In the rectifier circuit, the sinusoidal input voltage  $v_{rec}$  is equivalent to the load voltage  $v_L$  in the amplifier, and the dc load resistance  $R_{dc}$  is equivalent to the Thevenin equivalent resistance of the dc source in the amplifier ( $V_{DD}/I_0$ , where  $I_0$  is the dc

supply current). The passive components in both the amplifier and rectifier are ideally the same values, assuming that the efficiencies of the amplifier and rectifier are high.

Under optimum class-E operation, the input impedance of the rectifier at the switching frequency  $\omega_1$  can be found from the simplified circuit shown in Fig. 8(c). In the simplified circuit, the impedance of the switching network  $Z'_{rec}$  shown in Fig. 8(b) is replaced by a resistance  $R'_{rec}$  and reactance  $X'_{rec}$ , where  $Z'_{rec} = R'_{rec} + jX'_{rec}$ . Expressions for  $R'_{rec}$  and reactance  $X'_{rec}$  can be derived in terms of the switching duty cycle  $D$  and the switch resistance  $r_{DS}$  [37], [38]. The equations are

$$X'_{rec} = \frac{-1}{\pi} \left[ \frac{A_1 + A_2}{\omega C_P} + r_{DS} (A_3 + A_4) \right] \quad (8a)$$

$$R'_{rec} = 2(R_{dc} + r_{CH}) \sin^2 \phi_{rec} + 2A_5 r_{DS} + r_T \quad (8b)$$

where

$$A_1 = \pi(1 - D)[1 + 2 \sin(\phi_{rec}) \sin(\phi_{rec} - 2\pi D)] \quad (9a)$$

$$A_2 = \sin(2\pi D) + \frac{1}{4}[\sin(2\phi_{rec} - 4\pi D) - \sin(2\phi_{rec})] \quad (9b)$$

$$A_3 = \frac{1}{2} - \frac{\cos(2\phi_{rec})}{4} - \frac{\cos(2\phi_{rec} - 2\pi D)}{4} \quad (9c)$$

$$A_4 = -\sin(\phi_{rec}) \sin(\phi_{rec} - 2\pi D) \quad (9d)$$

$$A_5 = \frac{D}{2} + \frac{\sin(2\phi_{rec} - 4\pi D)}{8\pi} + D \sin^2(\phi_{rec}) - \frac{\sin(\phi_{rec}) \cos(\phi_{rec} - 2\pi D)}{\pi} + \frac{3 \sin(2\phi_{rec})}{8\pi} \quad (9e)$$

$$\phi_{rec} = \tan^{-1} \left[ \frac{1 - \cos(2\pi D)}{\sin(2\pi D) + 2\pi(1 - D)} \right] \quad (9f)$$

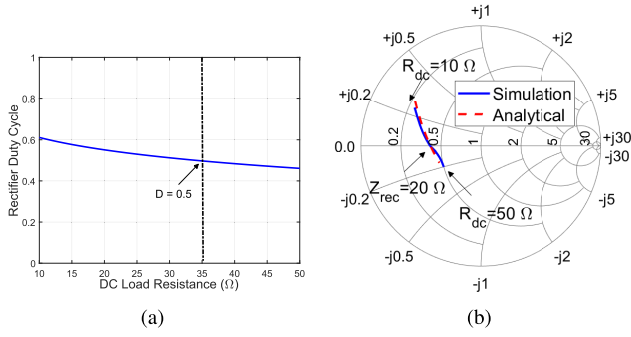


Fig. 10. (a) Plot shows how the rectifier duty cycle changes as a function of the dc load resistance  $R_{dc}$ . (b) Plot shows the input impedance of the 27.12-MHz class-E rectifier changes as a function of dc load resistance. The Smith chart is normalized to 50  $\Omega$  and shows both analytic and circuit simulation results.

In (8b), the resistance losses associated with finite inductor  $Q$  are included, where  $r_{CH}$  models the ac resistance of  $L_{CH}$  and  $r_T$  models the ac resistance of  $L_{SW}$  and  $L_T$ .

From the analysis, it can be seen that if reactive elements in the equivalent series resonant circuit shown in Fig. 8(c) are resonant at  $\omega_1$ , then the input impedance of the rectifier is purely resistive. On the other hand, if there are any changes to the rectifier circuit, such as a change in duty cycle that may be created by a change in the load resistance  $R_{dc}$ , then the rectifier input impedance is also reactive [39].

A sweep of the dc load resistance ( $R_{dc}$ ) from 10 to 50  $\Omega$  is shown in Fig. 10. When  $R_{dc}$  is equal to the exact Thevenin equivalent source resistance for the amplifier (35  $\Omega$ ), the rectifier duty cycle is 0.5, and the rectifier input impedance is purely real and equal to 20  $\Omega$  ( $R$ ). When  $R_{dc} < 35 \Omega$ , the rectifier input impedance becomes inductive, and when  $R_{dc} > 35 \Omega$ , the input impedance becomes capacitive. The reactive changes in impedance generated by changing the rectifier load resistance introduce limitations in the range over which load compensation can be used as a means for tracking changes in the gap distance in a CPT system, a point that is discussed further in Section VII.

A circuit diagram of the complete CPT system, including the class-E amplifier, the class-E rectifier, and an equivalent half-circuit model of the six-plate coupling link, is shown in Fig. 9. Unlike the amplifier circuit, which has an RF input source to switch the amplifier, the class-E rectifier circuit is self-synchronous and includes a feedback loop to generate an appropriately phased gate signal to synchronously switch transistor  $Q_2$ . The feedback network consists of a third-order Butterworth filter to generate a phase shift and attenuation and a pair of diodes,  $D_1$  and  $D_2$ , to clip the feedback signal to generate a switching input signal for the gate driver. Design values are summarized in Table III for 27.12 MHz and in Table IV for 13.56 MHz.

## VII. EXPERIMENTAL RESULTS AND DISCUSSION

In this section, the experimental verification of the proposed adaptive load and frequency-band-switching technique for impedance compensation is discussed. The experiments begin with individual system unit testing and conclude with an integrated CPT system test.

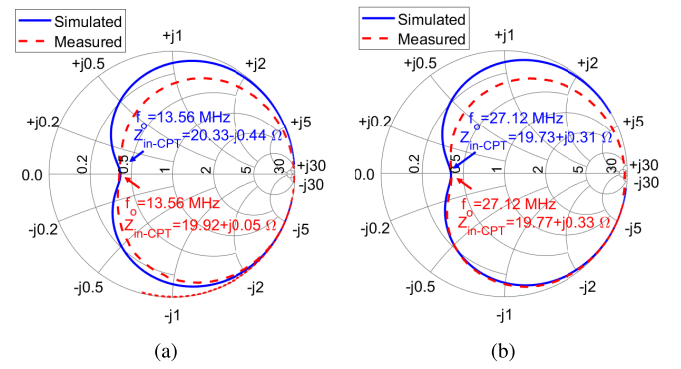


Fig. 11. Simulated and measured input reflection coefficient versus frequency for the CPT links. (a) Results for 13.56 MHz are shown. (b) Results for 27.12 MHz are shown. The normalized impedance is 50  $\Omega$ .

In the CPT link, the copper disk electrodes [1–4 in Fig. 2(a)] were isolated from the shield plates [5 and ground in Fig. 2(a)] using 6.35-mm (0.25") dielectric rods made of nylon. A copper wire is soldered to each disk and passes through a hole in the shield plates where it attaches to a terminal block. The terminal block is used to connect a series matching inductor and made it convenient to change the inductance for each frequency band. The terminal blocks add stray capacitance to the matching network, and the capacitance is shown as  $C_b$  in Fig. 9.

Matching inductors were wound on material 67 ferrite cores from Fair-Rite Products Corporation using solid 18 gauge copper wire. The cores have a relative permeability ( $\mu_r$ ) of approximately 40 over the ISM frequency bands of interest. Due to the toroidal shape of the cores and their high permeability, the majority of the magnetic fields are concentrated within the core, minimizing magnetic field emission and, consequently, reducing electromagnetic interference [40]. The inductor  $Q$  and self-resonant frequency ( $f_{sr}$ ) were measured with a Keysight PNA-X vector network analyzer (VNA). The  $Q$  values of the transmitter- and receiver-side inductors were measured to be 125.0 and 333.5, respectively, for the 13.56-MHz design and 123.4 and 147.7, respectively, for the 27.12-MHz design. The  $f_{sr}$  values of the transmitter- and receiver-side inductors were 41.5 and 55.9 MHz, respectively, for 13.56 MHz, and 86.0 and 118.5 MHz, respectively, for 27.12 MHz. From these measurements, the corresponding equivalent self-resonant capacitances ( $C_{sr}$ ) are 1.62 and 1.51 pF for the 13.56-MHz design and 1.16 and 1.13 pF for the 27.12-MHz design.

In the next step, the performance of the matched CPT link was verified. In the half-circuit model, both shielding plates (5 and 6) are at ground potential, and a copper braid was used to connect the shield plates together. The input impedance at the transmit port was measured with a 20- $\Omega$  load. Since a 20- $\Omega$  RF load was not readily available in the laboratory, an  $LC$  network was used to transform a 50- $\Omega$  load to 20  $\Omega$ . The impedance transformation was implemented with a variable capacitor and a fixed inductor.

The measured input impedance for 13.56 and 27.12 MHz is shown in Fig. 11(a) and (b). The results show that the input impedance is 20  $\Omega$  at a distance of 9.6 cm for the 27.12-MHz band and 13.6 cm for the 13.56-MHz band. Simulation results are also shown in Fig. 11(a) and (b) for comparison. For a



20- $\Omega$  input impedance, the simulation results had the critically coupled distances of 10.6 cm at 27.12 MHz and 14.0 cm at 13.56 MHz (see Fig. 6). The discrepancy between the simulated and measured critically coupled distances can be attributed to the stray capacitance  $C_b$  introduced by the terminal blocks. The terminal block adds approximately 2.5 pF of capacitance to each side of the matching inductors, as shown in Fig. 9, effectively increasing the capacitance in the transmit ( $C_{TX}$ ) and receive ( $C_{RX}$ ) resonators while keeping the mutual capacitance ( $C_m$ ) unchanged. As a result, the distance found in the experimental setup is slightly less than the COMSOL simulation results, which do not include the stray capacitance. Note that the larger discrepancy at 13.56 MHz relative to 27.12 MHz can be related to having a smaller coupling coefficient ( $K_C$ ).

The transmission efficiency of the CPT links was measured to be 67.4% at 13.56 MHz and 73.2% at 27.12 MHz. Using the efficiency expression  $[K_C^2 Q_1 Q_2] / [1 + (1 + K_C^2 Q_1 Q_2)^{1/2}]^2$ , the analytic values for power efficiency are 66.7% and 76.4% at 13.56 and 27.12 MHz, respectively, which are within 3% of the measured values. Note that these efficiency results are similar to those reported in other works in the literature [21] for the same frequency bands. The lower efficiency of the link at 13.56 MHz, despite having higher  $Q$  resonators, is attributed to its smaller coupling coefficient.

The class-E power amplifier and rectifiers were built on a 1.6-mm FR4 laminate. Inductors in the load and feedback networks were wound on Fair-Rite toroidal cores made of material 67 with an outer diameter of 0.87 in. All inductors used solid 18 gauge copper wires. Photographs of the amplifier and rectifier circuit boards are shown in Fig. 12(e) and (f).

System testing with the amplifier and rectifier began by first measuring the performance of the amplifier with a fixed 20- $\Omega$  load. The amplifiers were tested with a drain voltage ( $V_{DD1}$ ) of 10 V and an input pulse signal ( $v_p$ ) with a 50% duty cycle and a 0–4.8-V amplitude swing. The amplifier operating at 13.56 MHz had an output power of 1.7 W with an efficiency of 86.4%, while the 27.12-MHz amplifier had an output power of 1.6 W with an efficiency of 81.2%.

The class-E rectifiers were first tested in a back-to-back configuration with the amplifiers. The measured RF-to-dc efficiency of the rectifiers is 93.3% and 87.8% for 13.56 and 27.12 MHz, respectively. The rectifiers have slightly higher power efficiency than the amplifiers even though they are circuit duals. The slightly higher efficiency for rectifier circuits is consistent with other results published in the literature [41]. The primary difference between the circuits is the voltage–current region in which the active devices switch in the amplifiers and rectifiers. In the rectifiers, the FET switches turn off in the first quadrant and turn on in the third quadrant. On the other hand, in the PAs, the switches switch on and off in the first quadrant. The loss characteristics are different in the first and third quadrants of the voltage–current plane; consequently, the amplifier and rectifier have slightly different power efficiencies.

The next measurements that are discussed focus on the experimental verification of the proposed impedance compensation technique. To provide a baseline, the response of the

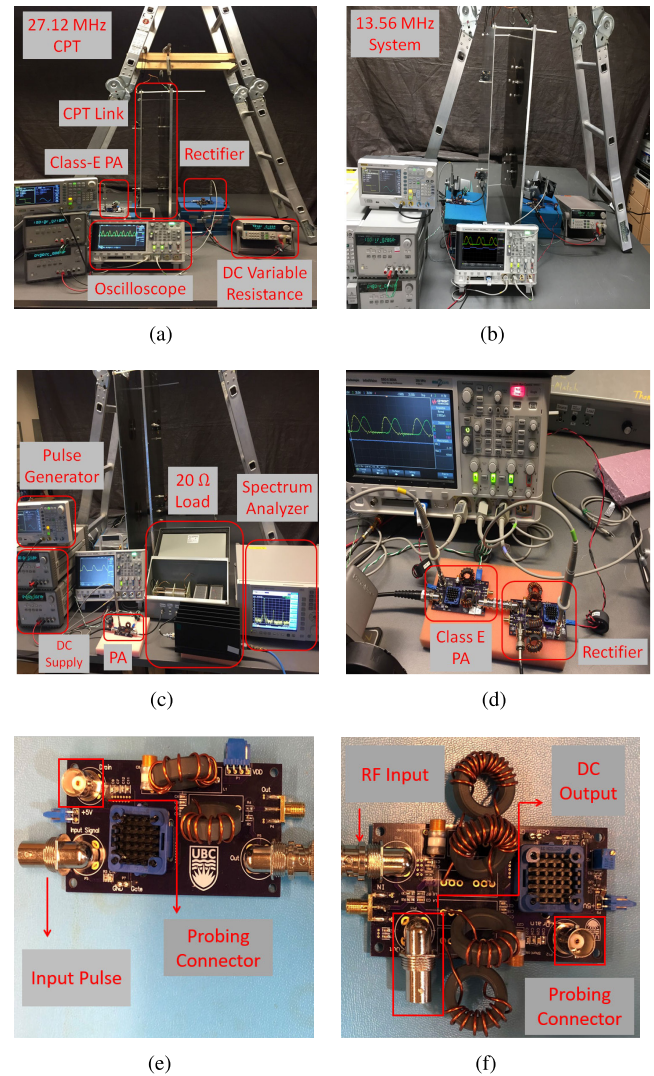


Fig. 12. Photographs of the measurement test benches. (a) 27.12-MHz test bench. The large rectangular shield plates are used to suspend the CPT electrodes from a ladder. The plate spacing was adjusted by sliding the plates on rollers that run in wooden tracks. (b) CPT system is configured with a 13.56-MHz amplifier and rectifier. (c) Test bench used to characterize the amplifier with a matched 20- $\Omega$  load. The load network consists of an LC match with a variable capacitance connected to a 50- $\Omega$  load. (d) Test bench used to measure the back-to-back performance of the class-E amplifier and rectifier. (e) Class-E amplifier is shown. (f) Class-E rectifier is shown.

system was measured with a fixed 20- $\Omega$  load and compared with the response of the system with an adjustable load. The separation distance was then varied from 2.6 to 14.6 cm at 27.12 MHz and from 2.6 to 18.6 cm at 13.56 MHz. The measured input resistance and reactance for a fixed 20- $\Omega$  load are shown in Fig. 13(a) for the 27.12-MHz link and Fig. 13(d) for the 13.56-MHz link. The results show that under a fixed load, the spatial bandwidth ( $\Delta g$ ) over which the magnitude of the input impedance is within  $20\ \Omega \pm 15\%$  is from 12.2 to 14.1 cm for 13.56 MHz and from 8.2 to 10.0 cm for 27.12 MHz. The fractional bandwidths normalized to the critical coupling distances ( $\Delta g/g_{opt}$ ) are 13.2% for 13.56 MHz and 18.7% for 27.12 MHz (see Table V).

The fixed-load results are now compared with the adjustable load results in Fig. 13. For example, in Fig. 13(a) and (d), the input impedance is within  $20\ \Omega \pm 15\%$  from 2.6 to 14.6 cm

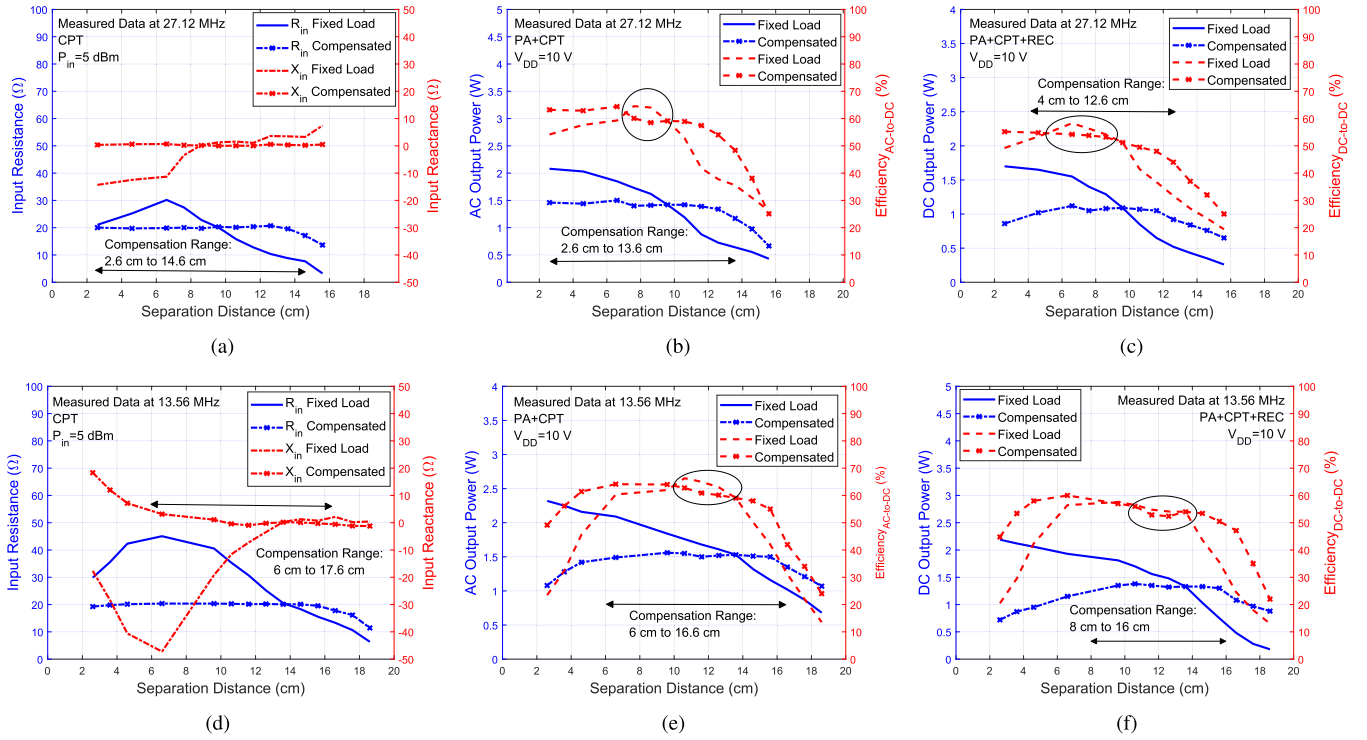


Fig. 13. Experimental results for CPT system tests. The top row shows results for 27.12 MHz, while the bottom row shows results for 13.56 MHz. (a) and (d) Input impedance is shown for the CPT link with fixed and adjustable loads. (b) and (e) Load power and overall system efficiency are shown for a CPT with a class-E power amplifier. (c) and (f) Load power and overall system efficiency are shown for a CPT system, including a class-E amplifier, CPT link, and a class-E rectifier.

TABLE V  
COMPENSATION RANGES FOR ADAPTIVE LOAD AND  
FREQUENCY-BAND-SWITCHING SYSTEMS

Setup	13.56 MHz		27.12 MHz	
	$\Delta g$	$\Delta g/g_{opt}$	$\Delta g$	$\Delta g/g_{opt}$
CPT	1.9 cm	13.2%	1.8 cm	18.7%
Comp. CPT	11.0 cm	80.9%	12.0 cm	125.0%
PA+CPT	2.6 cm	19.2%	1.2 cm	12.6%
Comp. PA+CPT	10.0 cm	73.5%	1.0 cm	121.2%
PA+CPT+REC	1.1 cm	8.1%	0.9 cm	8.64%
Comp. PA+CPT+REC	8.0 cm	58.9%	8.0 cm	83.3%

for 27.12 MHz and from 6.6 to 17.6 cm for 13.56 MHz. The fractional compensation ranges normalized to the critical coupling transmission distances are 80.9% for 13.56 MHz and 125.0% for 27.12 MHz. If band switching is employed to combine the additional benefit of using both load and frequency compensation, the operating range of the CPT link is extended to a range of 2.6–17.6 cm.

Next, the class-E amplifier was included in the verification of the load and frequency compensation methods. Measurements of the load power and overall power efficiency of the amplifier and CPT link are shown in Fig. 13(b) and (e). The output power and efficiency of the systems under a fixed-load condition are also included for comparison. Note that in the integrated systems, the compensation range ( $\Delta g$ ) is where the output power remains within 10% of the output power observed at the fixed-load critically coupled distance, while also maintaining an efficiency level above 75% of the efficiency achieved at that distance.

A significant benefit of compensation is to control the load power and system efficiency as gap distance varies. This is especially important to maintain a safe operating range for active devices in the class-E amplifier. Large changes in the peak voltage across the switch require large safety margins. This reduces the utilization of the power device by limiting the range of load power that can be delivered over a spatial channel with large impedance variation. On the other hand, with compensation, the impedance presented to the output of the amplifier is controlled, and operation is more predictable. Compensation, therefore, provides good control on regulating load power as well as maintains high efficiency.

From the compensation ranges marked in Fig. 13(b) and (e) and summarized in Table V, the load power is controlled over a range of 2.6–13.6 cm in the 27.12-MHz system and over a range of 6.0–16.6 cm in the system operating at 13.56 MHz. Uncompensated measurements with a fixed 20- $\Omega$  load are also shown, and the power varies significantly as separation distance changes. There are also short ranges where the efficiency of the overall system is slightly higher without compensation, which can occur when the class-E amplifier is operated in suboptimal modes [42], [43], [44]. However, the unregulated operation with a fixed load requires significantly more safety margins to ensure that the switching device does not fail. Therefore, regulated load power, which is obtained with compensation methods, significantly improves the robustness of the overall wireless power transfer system.

The last set of experiments verify the operation of an overall CPT system comprised of a class-E amplifier, CPT link, and class-E rectifier. The measurement test benches of both systems are shown in Fig. 12(a) and (b). The results are shown

in Fig. 13(c) and (f), where the dc load power and the overall dc-to-dc power efficiency of the end-to-end system are shown as a function of distance. The ranges where the dc output power is regulated with high efficiency are evident in both systems. The compensated ranges are 4.0–12.0 cm at 27.12 MHz and 8.0–16.0 cm at 13.56 MHz. Each frequency band provides a range of 8 cm, and the two compensated frequency ranges overlap by 4 cm. The dual-band configuration, therefore, extends the overall compensated range to 12 cm, which provides a range increase of 50% compared with a single-band system.

The compensated operating range of the overall system with an amplifier and rectifier is reduced compared with a system without an amplifier and rectifier (see Fig. 13(b) and (e) and Table V). The reduced compensation range is related to the mapping of the load resistance (purely real) to the rectifier input impedance (complex), which was shown earlier in Fig. 10(b). The rectifier input impedance is purely real ( $20\ \Omega$ ) for only one value of load resistance. Varying the dc load resistance generates both resistive and reactive changes at the input of the rectifier, which, in turn, affects the overall efficiency of the CPT system. A longer transmission distance range in the overall systems may be obtained by varying the value of the shunt capacitance ( $C_P$ ) across the switch in the class-E rectifier, but the complexity of the rectifier and the efficiency of the tuning circuit would all need to be evaluated to see if there is benefit from enhancements to the circuit.

### VIII. CONCLUSION

Frequency and load resistance can be used to compensate for spatial impedance changes in a CPT system. For practical systems that must be compliant with regulated spectral emissions, frequency compensation is constrained to narrow bandwidth ISM bands. Imposing the constraint that the system must operate in discrete frequency bands, this article investigated the merits of employing a spatial impedance compensation system that changes both frequency and load resistance.

Several conclusions are made from this study. First, load resistance changes can be highly effective over modest spatial changes. A theoretical explanation for how load compensation works was given by reducing the capacitive coupling link to an impedance inverter where the inverter impedance is spatially dependent. Since the load is typically a rectifier, a supporting analysis of how a change in load resistance modifies the input impedance of the rectifier was presented. The load change creates both resistance and reactive changes in input impedance; therefore, the range of impedance compensation is also dependent on the rectifier circuit.

Second, multiband operation can provide substantial improvements in the spatial range over which the system can maintain constant load power. Compared with a single-band system, the dual-band system increased the compensated gap range by 50%. These results demonstrate that the combination of frequency band switching and adaptive load can be used to obtain robust power transfer over a large range in gap distances.

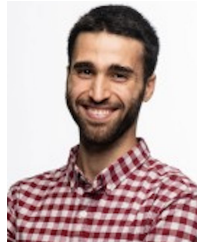
Third, a multiband system is more complex than a single-band system; therefore, the method that is used for spatial impedance compensation depends on what the requirements are for the application of the technology. If a very robust and spatially variable application is required, then multiband adaptive load compensation offers significant advantages in maintaining constant load power over highly variable conditions. On the other hand, if the application has modest spatial variation, with well-defined range constraints, then single-band adaptive load compensation is likely to be sufficient.

### REFERENCES

- [1] N. Y. Kim, K. Y. Kim, J. Choi, and C.-W. Kim, "Adaptive frequency with power-level tracking system for efficient magnetic resonance wireless power transfer," *Electron. Lett.*, vol. 48, no. 8, pp. 452–454, Apr. 2012.
- [2] A. P. Sample, D. T. Meyer, and J. R. Smith, "Analysis, experimental results, and range adaptation of magnetically coupled resonators for wireless power transfer," *IEEE Trans. Ind. Electron.*, vol. 58, no. 2, pp. 544–554, Feb. 2011.
- [3] Y. Zhang, Z. Zhao, and K. Chen, "Frequency-splitting analysis of four-coil resonant wireless power transfer," *IEEE Trans. Ind. Appl.*, vol. 50, no. 4, pp. 2436–2445, Jul. 2014.
- [4] Y. Li et al., "Improved ant colony algorithm for adaptive frequency-tracking control in WPT system," *IET Microw., Antennas Propag.*, vol. 12, no. 1, pp. 23–28, Jan. 2018.
- [5] X. Liu, X. Yuan, C. Xia, and X. Wu, "Analysis and utilization of the frequency splitting phenomenon in wireless power transfer systems," *IEEE Trans. Power Electron.*, vol. 36, no. 4, pp. 3840–3851, Apr. 2021.
- [6] D. Zhigang, C. Yuan, and J. A. A. Qahouq, "Reconfigurable magnetic resonance-coupled wireless power transfer system," *IEEE Trans. Power Electron.*, vol. 30, no. 11, pp. 6057–6069, Nov. 2015.
- [7] T. C. Beh, M. Kato, T. Imura, S. Oh, and Y. Hori, "Automated impedance matching system for robust wireless power transfer via magnetic resonance coupling," *IEEE Trans. Ind. Electron.*, vol. 60, no. 9, pp. 3689–3698, Sep. 2013.
- [8] C. Liu, A. P. Hu, G. A. Covic, and N. C. Nair, "Comparative study of CCPT systems with two different inductor tuning positions," *IEEE Trans. Power Electron.*, vol. 27, no. 1, pp. 294–306, Jan. 2012.
- [9] J. James, J. Boys, and G. Covic, "A variable inductor based tuning method for ICPT pickups," in *Proc. Int. Power Eng. Conf.*, Nov. 2005, pp. 1142–1146.
- [10] O. Abdelatty, X. Wang, and A. Mortazawi, "Position-insensitive wireless power transfer based on nonlinear resonant circuits," *IEEE Trans. Microw. Theory Techn.*, vol. 67, no. 9, pp. 3844–3855, Sep. 2019.
- [11] S. Shekhar, S. Mishra, and A. Joshi, "A utility interfaced half-bridge based capacitively coupled power transfer circuit with automatic frequency control," in *Proc. IEEE Energy Convers. Congr. Expo.*, Sep. 2013, pp. 1598–1602.
- [12] S. Sinha, A. Kumar, B. Regensburger, and K. K. Afridi, "Active variable reactance rectifier—A new approach to compensating for coupling variations in wireless power transfer systems," *IEEE J. Emerg. Sel. Topics Power Electron.*, vol. 8, no. 3, pp. 2022–2040, Sep. 2020.
- [13] A. Kumar, S. Sinha, and K. K. Afridi, "A high-frequency inverter architecture for providing variable compensation in wireless power transfer systems," in *Proc. IEEE Appl. Power Electron. Conf. Expo. (APEC)*, Mar. 2018, pp. 3154–3159.
- [14] Y. Narusue, Y. Kawahara, and T. Asami, "Maximum efficiency point tracking by input control for a wireless power transfer system with a switching voltage regulator," in *Proc. IEEE Wireless Power Transf. Conf. (WPTC)*, May 2015, pp. 1–4.
- [15] A. Berger, M. Agostinelli, S. Vesti, J. A. Oliver, J. A. Cobos, and M. Huemer, "A wireless charging system applying phase-shift and amplitude control to maximize efficiency and extractable power," *IEEE Trans. Power Electron.*, vol. 30, no. 11, pp. 6338–6348, Nov. 2015.
- [16] M. Fu, H. Yin, M. Liu, and C. Ma, "Loading and power control for a high-efficiency class E PA-driven megahertz WPT system," *IEEE Trans. Ind. Electron.*, vol. 63, no. 11, pp. 6867–6876, Nov. 2016.
- [17] M. Fu, H. Yin, X. Zhu, and C. Ma, "Analysis and tracking of optimal load in wireless power transfer systems," *IEEE Trans. Power Electron.*, vol. 30, no. 7, pp. 3952–3963, Jul. 2015.

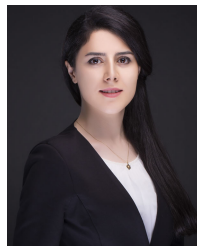


- [18] L. Murliky, R. W. Porto, V. J. Brusamarello, F. R. de Sousa, and A. Triviño-Cabrera, "Active tuning of wireless power transfer system for compensating coil misalignment and variable load conditions," *AEU Int. J. Electron. Commun.*, vol. 119, May 2020, Art. no. 153166.
- [19] H. Li, J. Fang, S. Chen, K. Wang, and Y. Tang, "Pulse density modulation for maximum efficiency point tracking of wireless power transfer systems," *IEEE Trans. Power Electron.*, vol. 33, no. 6, pp. 5492–5501, Jun. 2018.
- [20] W. X. Zhong and S. Y. R. Hui, "Maximum energy efficiency tracking for wireless power transfer systems," *IEEE Trans. Power Electron.*, vol. 30, no. 7, pp. 4025–4034, Jul. 2015.
- [21] C. Lu et al., "Design and analysis of an omnidirectional dual-band wireless power transfer system," *IEEE Trans. Antennas Propag.*, vol. 69, no. 6, pp. 3493–3502, Jun. 2021.
- [22] M.-L. Kung and K.-H. Lin, "Enhanced analysis and design method of dual-band coil module for near-field wireless power transfer systems," *IEEE Trans. Microw. Theory Techn.*, vol. 63, no. 3, pp. 821–832, Mar. 2015.
- [23] D. Ahn and P. P. Mercier, "Wireless power transfer with concurrent 200-kHz and 6.78-MHz operation in a single-transmitter device," *IEEE Trans. Power Electron.*, vol. 31, no. 7, pp. 5018–5029, Jul. 2016.
- [24] Z. Ye, M. Yang, and P.-Y. Chen, "Multi-band parity-time-symmetric wireless power transfer systems for ISM-band bio-implantable applications," *IEEE J. Electromagn., RF Microw. Med. Biol.*, vol. 6, no. 2, pp. 196–203, Jun. 2022.
- [25] M.-L. Kung and K.-H. Lin, "A 6.78 MHz and 13.56 MHz dual-band coil module with a repeater for wireless power transfer systems," in *Proc. IEEE Int. Symp. Antennas Propag. (APSURSI)*, Jun. 2016, pp. 157–158.
- [26] M. Liu and M. Chen, "Dual-band multi-receiver wireless power transfer: Architecture, topology, and control," *IEEE Trans. Power Electron.*, vol. 35, no. 1, pp. 496–507, Mar. 2019.
- [27] M. Ahmadi, L. Markley, and T. Johnson, "A filter theory approach to the synthesis of capacitive power transfer systems," *IEEE J. Emerg. Sel. Topics Power Electron.*, vol. 10, no. 1, pp. 91–103, Feb. 2022.
- [28] A. Clements, R. McDonald, M. Ahmadi, and T. Johnson, "Design method for differentially-driven capacitive wireless power transfer systems," in *Proc. IEEE Wireless Power Transf. Conf. (WPTC)*, Nov. 2020, pp. 292–295.
- [29] A. Zverev, *Handbook of Filter Synthesis*, 1st ed. New York, NY, USA: Wiley, 1967, Ch. 6, p. 291.
- [30] C.-M. Tsai and H.-M. Lee, "The effects of component Q distribution on microwave filters," *IEEE Trans. Microw. Theory Techn.*, vol. 54, no. 4, pp. 1545–1553, Jun. 2006.
- [31] M. Oldoni, G. Macchiarella, G. G. Gentili, and C. Ernst, "A new approach to the synthesis of microwave lossy filters," *IEEE Trans. Microw. Theory Techn.*, vol. 58, no. 5, pp. 1222–1229, May 2010.
- [32] L. Weinberg, "Additional tables for design of optimum ladder networks," *J. Franklin Inst.*, vol. 264, no. 1, pp. 7–23, Jul. 1957.
- [33] G. Matthaei, L. Young, and E. Jones, "Design of microwave filters, impedance-matching networks, and coupling structures," Stanford Res. Inst., Menlo Park CA, USA, Tech. Rep., 1963, Ch. 4, pp. 104–105, vol. 1.
- [34] B. Luo, S. Wu, and N. Zhou, "Flexible design method for multi-repeater wireless power transfer system based on coupled resonator bandpass filter model," *IEEE Trans. Circuits Syst. I, Reg. Papers*, vol. 61, no. 11, pp. 3288–3297, Nov. 2014.
- [35] D. C. Hamill, "Time reversal duality and the synthesis of a double class E DC–DC converter," in *Proc. 21st Annu. IEEE Conf. Power Electron. Spec.*, Aug. 1990, pp. 512–521.
- [36] *Enhancement Mode Power Transistor*, document EPC2037, Efficient-Power-Conversion, El Segundo, CA, USA, 2020.
- [37] M. Liu, M. Fu, and C. Ma, "Parameter design for a 6.78-MHz wireless power transfer system based on analytical derivation of class E current-driven rectifier," *IEEE Trans. Power Electron.*, vol. 31, no. 6, pp. 4280–4291, Jun. 2016.
- [38] A. Ivagcu, M. K. Kazimierzczuk, and S. Birca-Galateanu, "Class E resonant low du/dt rectifier," *IEEE Trans. Circuits Syst. I, Fundam. Theory Appl.*, vol. 39, no. 8, pp. 1–10, Aug. 1992.
- [39] M. Ahmadi, "Impedance compensation methods in wireless power transfer systems under variable coupling conditions," Ph.D. dissertation, School Eng., Univ. British Columbia, Kelowna, BC, Canada, 2023.
- [40] B. Zhang and S. Wang, "Analysis and reduction of the near magnetic field emission from toroidal inductors," *IEEE Trans. Power Electron.*, vol. 35, no. 6, pp. 6251–6268, Jun. 2020.
- [41] S. Abbasian and T. Johnson, "Power-efficiency characteristics of class-F and inverse class-F synchronous rectifiers," *IEEE Trans. Microw. Theory Techn.*, vol. 64, no. 12, pp. 4740–4751, Dec. 2016.
- [42] N. O. Sokal and A. D. Sokal, "Class E—A new class of high-efficiency tuned single-ended switching power amplifiers," *IEEE J. Solid-State Circuits*, vol. SSC-10, no. 3, pp. 168–176, Jun. 1975.
- [43] F. Raab, "Suboptimum operation of class-E RF power amplifiers," in *Proc. RF Technol. Expo.*, vol. 89, 1989, pp. 85–98.
- [44] F. J. Ortega-Gonzalez, D. Tena-Ramos, M. Pati no-Gomez, J. M. Pardo-Martin, and D. Madue no-Pulido, "High-power wideband L-band suboptimum class-E power amplifier," *IEEE Trans. Microw. Theory Techn.*, vol. 61, no. 10, pp. 3712–3720, Oct. 2013.



**Masoud Ahmadi** received the M.A.Sc. and Ph.D. degrees in electrical engineering from the University of British Columbia, Kelowna, BC, Canada, in 2018 and 2023, respectively.

Presently, he serves as a Hardware Engineer at AleaSat Inc. and Rogers Communications. Within AleaSat, his focus lies on satellite communication systems, while at Rogers Communications, he is dedicated to the development of wearable devices for vital sign measurement. Previously, his research concentrated primarily on novel antenna structures, radio frequency integrated circuits (RFIC), wireless power transfer (WPT) systems, sensors, embedded systems, and applied electromagnetics.



**Hoda Dadashzadeh** received the B.Sc. degree in electrical engineering from the University of Tabriz, Tabriz, Iran, in 2017, and the M.A.Sc. degree from The University of British Columbia, Kelowna, BC, Canada, in 2022, with a focus on RF power amplifiers and rectifiers.

She is currently a Hardware Developer with the Department of Research and Development, Fortinet, Burnaby, BC, Canada. Her primary research interests include the design of transmitters–receivers for wireless power systems and design of high-speed circuits.



**Loïc Markley** (Senior Member, IEEE) received the B.A.Sc. degree in electronics engineering from Simon Fraser University, Burnaby, BC, Canada, in 2004, and the M.A.Sc. and Ph.D. degrees in electrical engineering from the University of Toronto, Toronto, ON, Canada, in 2007 and 2013, respectively.

He is currently an Associate Professor with the School of Engineering, The University of British Columbia, Kelowna, BC, Canada. His research interests include applied electromagnetics, artificial dielectrics and metamaterials, transmission-line structures, passive microwave circuits, frequency-selective surfaces, leaky-wave antennas, and wireless power transfer.

Dr. Markley was a recipient of the Tatsuo Itoh Best Paper Award for his paper on near-field focusing published in IEEE MICROWAVE AND WIRELESS COMPONENTS LETTERS in 2010. From 2015 to 2020, he served as an Associate Editor for IEEE ANTENNAS AND WIRELESS PROPAGATION LETTERS.



**Thomas Johnson** (Member, IEEE) received the B.A.Sc. degree in electrical engineering from The University of British Columbia (UBC), Kelowna, BC, Canada, in 1987, and the M.A.Sc. and Ph.D. degrees from Simon Fraser University, Burnaby, BC, Canada, in 2001 and 2007, where he focused on research in RF and microwave power amplifiers.

In 2009, he was a Technical Lead in a number of high-tech companies, including PulseWave RF, Austin, TX, USA, ADC Telecommunications, Vancouver, BC, Canada, and Norsat International Richmond, BC, Canada. He is currently an Associate Professor with the School of Engineering, UBC. His research interests include the design of radio frequency circuits and systems, wireless power systems, wireless sensors, and industrial applications of RF/microwave power.